



Cite this: *Nanoscale*, 2015, 7, 19053

Routing of surface plasmons in silver nanowire networks controlled by polarization and coating

Hong Wei,^{*a} Deng Pan^a and Hongxing Xu^{*a,b}

Controllable propagation of electromagnetic energy in plasmonic nanowaveguides is of great importance for building nanophotonic circuits. Here, we studied the routing of surface plasmons in silver nanowire structures by combining experiments and electromagnetic simulations. The superposition of different plasmon modes results in the tunable near field patterns of surface plasmons on the nanowire. Using the quantum dot fluorescence imaging technique, we experimentally demonstrate that the near field distribution on the nanowire controls the surface plasmon transmission in the nanowire networks. By controlling the polarization of the input light or by controlling the dielectric coating on the nanowire to modulate the plasmon field distribution and guarantee the strong local field intensity at the connecting junction, the surface plasmons can be efficiently routed to the connected nanowires. Depositing a thin layer of Al₂O₃ film onto the nanowires can reverse the polarization dependence of the output intensity at the nanowire terminals. These results are instructive for designing functional plasmonic nanowire networks and metal-nanowire-based nanophotonic devices.

Received 17th April 2015,
Accepted 29th September 2015

DOI: 10.1039/c5nr02511g

www.rsc.org/nanoscale

Introduction

Metal nanostructures show many valuable properties based on surface plasmons (SPs),¹ among which the SP propagation in one dimensional nanostructures has attracted much attention in recent years because it provides a promising avenue towards the optical interconnects with electronic devices and the construction of plasmonic circuits.² Among the various structures investigated as plasmonic waveguides,^{3–8} silver nanowires (Ag NWs) prepared by chemical synthesis are used in many research studies due to their crystalline structure that results in the small loss of propagating SPs in the visible to near infrared spectral range.^{9–12} Many fundamental properties of SPs in Ag NWs have been revealed,^{13–15} such as the emission direction,^{16–19} polarization,^{20,21} loss,^{22–26} group velocity,^{27,28} interference,^{29–32} routing and spectral splitting,^{33–35} modulation,^{35,36} photon-plasmon coupling efficiency,^{37,38} and coupling with semiconductor NWs and quantum emitters.^{39–48} It is demonstrated that branched NW structures in a homogeneous environment can be used as routers and demultiplexers to split SPs into different NW branches.³³ To get a deeper understanding of the SP propagation behavior in NWs and thus to enable the rational design of controllable SP routing, it is highly desirable to experi-

mentally measure the plasmon field distributions. Recently, we developed a quantum dot (QD) fluorescence imaging technique for NW SPs,³⁰ which utilizes the energy transfer between plasmons and excitons to excite the QDs by propagating SPs.⁴³ By using this technique, the plasmon field distributions can be conveniently obtained using the normal optical microscope.

Here we investigate the surface plasmon transmission in Ag NW networks by analyzing the plasmon modes and imaging the plasmon field. The coherent superposition of different plasmon modes results in specific near field patterns of propagating SPs on the NW. It's found that the near field distribution plays a central role in determining the routing behavior in Ag NW networks. By tuning the polarization of the excitation light or by coating a thin layer of Al₂O₃ onto the NW, the output intensity at different output terminals is changed. The polarization dependence of the output intensity can be reversed by depositing an Al₂O₃ layer of 10 nm thickness. The near field intensity distributions revealed by QD imaging show that, when the local field intensity at the junction of the branch wire is strong, SPs can be more efficiently routed to that wire. The dependence of the SP routing behavior on the near field distribution makes it designable to manage SP transmission in nanophotonic circuits composed of plasmonic waveguides.

Experimental and theoretical methods

Crystalline silver nanowires were chemically synthesized according to the method in the literature,⁴⁹ and washed in

^aBeijing National Laboratory for Condensed Matter Physics, Institute of Physics, Chinese Academy of Sciences, Beijing 100190, China. E-mail: weihong@iphy.ac.cn

^bCenter for Nanoscience and Nanotechnology, School of Physics and Technology, and Institute for Advanced Studies, Wuhan University, Wuhan 430072, China. E-mail: hxXu@whu.edu.cn

ethanol by centrifugation. The ethanol suspension containing Ag nanowires was dropped onto a clean glass substrate, and dried naturally. The nanowire networks composed of several NWs were assembled by using a micromanipulator mounted on an upright optical microscope. A layer of 30 nm thickness Al_2O_3 was deposited on the sample using an atomic layer deposition (ALD) system. Finally, quantum dots (Invitrogen, catalog number Q21321MP) were spin-coated on top of the sample surface. The Al_2O_3 layer can function as a spacer layer between the Ag NW and the QDs to prevent the QD fluorescence quenching caused by the Ag wire. Moreover, the Al_2O_3 layer becomes a part of the nanowire waveguide as the Ag NW and the Al_2O_3 layer form a quasi core-shell structure. In addition, the Al_2O_3 layer protects the Ag NWs from oxidization and makes the waveguide structures very stable. The optical measurements were carried out on an upright optical microscope. Laser light of 633 nm wavelength from a He-Ne laser was focused onto the NW through a 100 \times objective to excite the propagating SPs. The emission light from the NW was collected by the same objective and directed to a CCD camera. A half-wave plate was used to change the polarization of the excitation light. To detect the QD fluorescence, a long-pass edge filter was inserted to block the laser light.

Numerical simulations are used to uncover the underlying physics and reproduce the experimental observations. The physical understanding is obtained based on the analyses of the eigenmodes supported by the NW structure, using finite element method (FEM) calculations. The FEM is convenient to calculate the mode profiles for a given 2-dimensional waveguide geometry. Using single or several obtained modes as the input for 3-dimensional calculation, the propagation behavior of the individual modes and their superposition are clearly observed. The finite-difference time-domain (FDTD) method is applied to reproduce the experimental observations in the structures of large scale and complicated geometry. The geometry in the simulation is modeled with parameters according to the structures in experiments. Non-uniform mesh grids with a size of 4 nm near the NW along with an adjusted size of simulation region guarantee good convergence. In all the simulations, interpolation of experimental result is used for the complex permittivity of silver ($-18.34 + 0.5i$ for 633 nm wavelength).⁵⁰ The refractive indexes of the SiO_2 and Al_2O_3 used in the simulation are 1.5 and 1.62, respectively.

Results and discussion

Mode determined plasmon propagation patterns

The instant surface charge and field distribution for plasmon modes as well as their superposition on the surface of a NW in a homogeneous dielectric environment ($n = 1.5$) are shown in Fig. 1(a). The first three rows in Fig. 1(a) show the three lowest order modes of the propagating SPs on the NW. The order of mode is decided by the azimuthal quantum number m . The fundamental mode ($m = 0$) is the transverse magnetic mode,

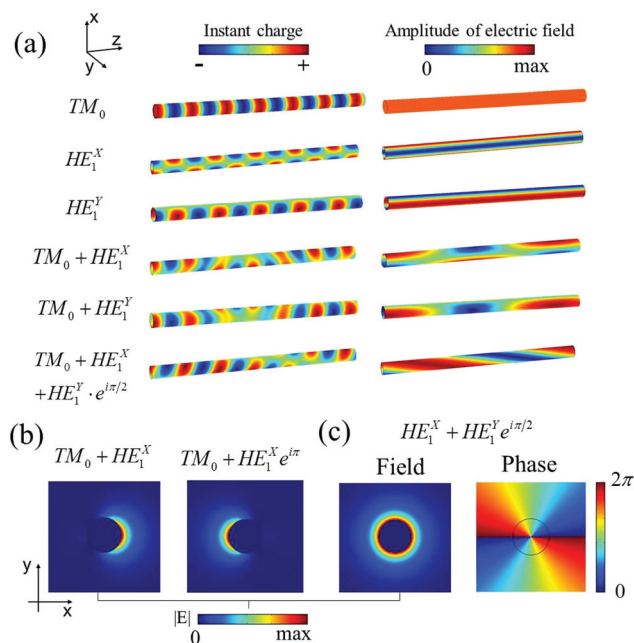


Fig. 1 (a) Distributions of instant charges and amplitude of electric field on the Ag NW surface for different eigenmodes and their superpositions. The radius of the NW is 60 nm and the section shown is 2 μm long. In the simulation, the solved eigenmodes for the cylindrical NW and their superpositions are directly used as the excitation source at the left boundary, and the propagating SPs are perfectly absorbed with no reflection at the right boundary. The expressions in the left column denote the superposition of modes with relative phase difference at the input port. The phase difference will further accumulate during the propagation. The zero phases are taken for TM_0 and HE_1^x when the electric field reaches the maximum along the positive direction of the x axis and for HE_1^y when the electric field reaches the maximum along the positive direction of the y axis. For the excitations by individual eigenmodes in the three upper rows, due to the perfect absorption of the boundary, the distributions of the field amplitude are uniform along the propagation. For the interference of eigenmodes of different orders, the distributions of the field amplitude show zigzag (fourth and fifth rows) and chiral (lowest row) shapes. (b) Field amplitude for the superposition of TM_0 mode and HE_1^x mode, with relative phase difference of 0 (left) and π (right). (c) Field amplitude and phase for the superposition of HE_1^x mode and HE_1^y mode, with HE_1^y bringing a phase lead of $\pi/2$.

denoted as TM_0 . For TM_0 mode, the charges oscillate along the NW and the electric field in the x-y plane is radially polarized, with field intensity axisymmetrically distributed on the surface of the wire. Two higher order ($m = 1$) modes are doubly degenerate hybrid modes, with charges oscillating in the x or y direction (denoted as HE_1^x or HE_1^y respectively). The HE_1 modes resemble linear polarization, with the electric field aligned nearly in the same direction and their field intensity distributed separately on the two sides of the NW.

The superposition of the fundamental TM_0 mode and an $m = 1$ mode with the same maximum intensity is shown in the fourth and fifth rows. As can be seen, the superposed field propagates in zigzag routes. When both of the modes have their field amplitudes reaching the maximum, considering the polarization characteristic of the two modes, they will interfere

constructively and destructively separately on the two sides of the nanowire, as shown in Fig. 1(b). The two modes have different effective refractive indexes, so along the propagation they will accumulate different phases. When the phase difference reaches π , the maximum of the field intensity will move from one side of the wire to the other side. Further propagation will pull the intensity maximum back and such repetition results in a zigzag route. The superposition of two degenerate $m = 1$ modes with no phase difference is of no significance, as it is just the same as the HE_1 mode with a rotation. When the two modes have a phase difference of $\pi/2$, the superposition is much more interesting owing to its chirality. As shown in Fig. 1(c), the superposed field becomes axisymmetric with a helical phase front, similar to the beam in free space with orbital momentum.⁵¹ Furthermore, an additional TM_0 mode component will make the field distribution more exotic.²¹ As shown in the sixth row in Fig. 1(a), the superposed field shows a helix distribution, with the chirality determined by the relative phase between two $m = 1$ modes.

In experiments, the excitation of these plasmon modes on NW can be achieved by inputting light at the end of the NW. For input light incident along the direction opposite to y , the polarization along the z direction will excite the TM_0 mode (and the HE_1^y mode due to retardation effect), and the polarization along the x direction will excite the HE_1^x mode. The chiral pattern due to the excitation of the three lowest order modes can be experimentally observed by using the QD fluorescence imaging technique. Fig. 2(a) shows the scanning electron microscopy (SEM) image of a QD-decorated Ag NW on a glass substrate. By immersing the NW into refractive-index-matching oil, the dielectric environment of the NW becomes homogeneous. The propagating plasmons can be launched by focusing laser light of 633 nm wavelength onto the end of the NW (Fig. 2(b)). The plasmons reaching the distal end of the NW couple out as photons with the output efficiency determined by the NW structure.⁴⁴ The QD fluorescence images (Fig. 2(c) and (d)) indicate the field distributions of helical plasmons on the NW with the chirality dependent on the polarization of the excitation light. The experimental results are reproduced in simulations as shown in Fig. 2(e) and (f). In Fig. 2(g) and (h), we also show the near field distributions for the SPs when the polarization of the Gaussian beam is parallel and perpendicular to the NW, respectively. For the parallel excitation, the TM_0 mode and the HE_1^y mode are generated simultaneously and their interference leads to the symmetric periodic distribution. For the perpendicular excitation, only the HE_1^x mode can be excited and the field is distributed on the two sides of the NW. The dependence of the plasmon field on excitation polarization provides a means to control the plasmon transmission to other connected structures in nanophotonic circuits. It should be noted that the homogeneous surrounding medium of the NW is critical for observing the ideal chiral plasmons.

Polarization controlled plasmon scattering and routing

For applications in nanophotonic circuits, the nanowire waveguides are supported by substrates and the surrounding

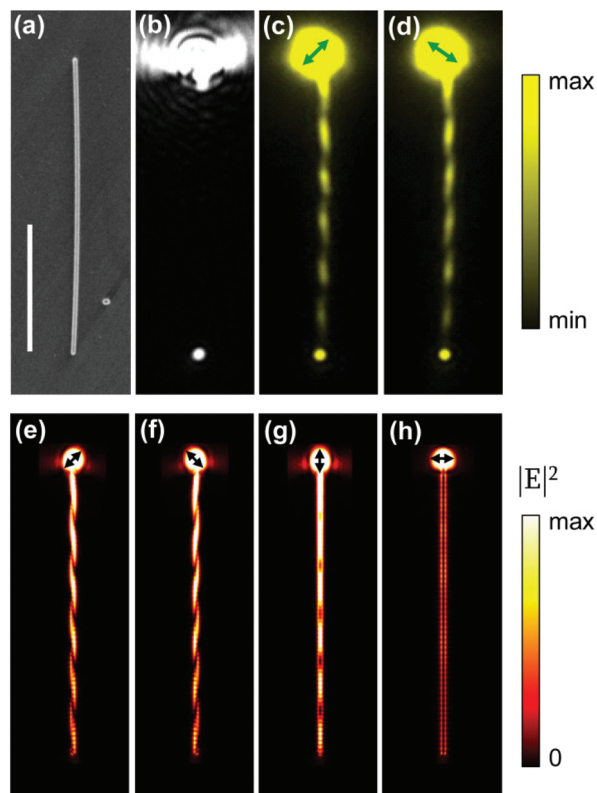


Fig. 2 (a) SEM image of an Ag NW. The length of the scale bar is 5 μm . The NW radius is about 65 nm, and Al_2O_3 thickness is 10 nm. (b) Scattering image for laser light focused on the top end of the NW. (c, d) QD fluorescence images for different laser polarizations indicated by the green arrows. (e–h) Simulation results by the FEM method for the experimental Ag NW under excitation of different polarizations indicated by the arrows. In the simulation, a Gaussian beam with a waist of 400 nm is incident onto the end of an Ag NW of 65 nm radius and 11.7 μm long. In order to be consistent with the experiment, the NW is covered by a 10 nm-thick Al_2O_3 shell ($n = 1.62$) and then placed in a uniform environment ($n = 1.5$). Here the field is shown for the section across the center of the NW. But for the section inside the Al_2O_3 and the NW, the outer surface of the Al_2O_3 layer is used instead. So the field is shown for the combined 3-dimensional surface viewed along the incident direction of the Gaussian beam.

medium is usually quite asymmetric. Compared with the NW in a homogeneous environment, the field profiles of plasmon modes on the substrate-supported NW become different. However, the near field distribution on the NW is still the result of coherent superposition of multiple modes. The asymmetry of the dielectric surroundings makes the helical propagating route in a uniform environment partly disturbed. The near field distribution of a substrate-supported NW is still strongly dependent on the polarization of excitation light. Fig. 3(a) shows a system composed of a single Ag NW and a few Ag nanoparticles (NPs). The QD fluorescence image by wide field excitation in Fig. 3(b) shows the NW was covered homogeneously by QDs. Propagating SPs were launched at the left end of the NW by focused laser light. With the tuning of the laser polarization, the brightness of the three NPs

(A, B and C) is changed (Fig. 3(c)i–iii). The QD fluorescence along the NW shows polarization-dependent zig-zag distribution patterns (Fig. 3(d)), which are formed by the superposition of different plasmon modes.^{21,35,52}

For clarity, NPs A and C are marked by yellow arrows. For the polarization shown in Fig. 3(c)i, NP A shows a strong scattering while NP C is dark. From Fig. 3(d)i, it can be seen that the near field at the NP A position is strong, and for NP C, the electric field is distributed on the top side of the NW, which can be seen more clearly in the inset image shown at the bottom corresponding to the part in the yellow rectangle. As the incident polarization is rotated clockwise to the direction in Fig. 3(c)ii, the scattering intensity of NP A is decreased and NP C becomes bright. The QD emission image in Fig. 3(d)ii shows the change of near field distribution compared with Fig. 3(d)i. And the near field intensities at the positions of NPs A and C are similar. As the incident polarization is rotated further (Fig. 3(c)iii), NP A becomes dark and NP C scatters strongly. It's shown in Fig. 3(d)iii that the plasmon field has been shifted to the NP C position. Fig. 3(e) shows the polarization-dependent light intensity scattered by the three NPs, from which the opposite polarization dependence of NPs A and C can be clearly seen. Fig. 3(c) and (e) also show that the polarization dependence of NP B is opposite to that of NP A. Because these two NPs are located on two adjacent plasmon field periods, when the plasmon field at NP A is strong, the field at B is weak due to the zig-zag distribution, and *vice versa*. The zig-zag field distribution also determines the same

polarization dependence for NPs B and C that are located on opposite sides of the NW. From these results, it can be concluded that the incident polarization determines the near field distribution, and the near field distribution determines the particle scattering intensity. Thus, by controlling the incident laser polarization, the light intensity scattered by the particles can be well controlled.

If the nanoparticle is extended to a nanowire, a branched nanostructure is formed. For the branched structure in Fig. 4(a), the laser was focused on the top end of the main wire to launch the propagating SPs, which coupled out at the main wire end O1 and the branch wire end O2. For the polarization shown in Fig. 4(b), the scattered light intensity at terminal O2 is strong, while the intensity at terminal O1 is weaker. When the laser polarization was rotated to the direction shown in Fig. 4(c), the light intensity at O2 became very weak, and the light intensity at O1 was strong. Since the plasmons launched at the top end of the main wire transmit to the branch wire through the junction, the near field distribution at the junction plays an important role in determining the direction of the plasmon transmission. QD fluorescence imaging was used to detect the near field distribution in this branched NW structure. For the laser polarization shown in Fig. 4(d), the strong near field is partly overlapped with the branch junction, that is, the local electric field intensity at the junction is strong. Thus, a large part of the plasmons will transmit to the branch wire, resulting in stronger emission intensity at the O2 end (Fig. 4(b)). When the laser polarization was rotated to the direction shown in Fig. 4(e), the near field is distributed along the two sides of the main wire with a clear zig-zag pattern. At the junction position, the near field antinode is located at the left side of the NW, so less plasmons can transmit to the branch wire, which determines the weak emission intensity at O2.

For the glass-supported Al_2O_3 -coated Ag NWs, the strong dependence of near field distribution on the polarization of excitation light can also be understood from the perspective of mode superposition, similar to the NWs in the homogeneous

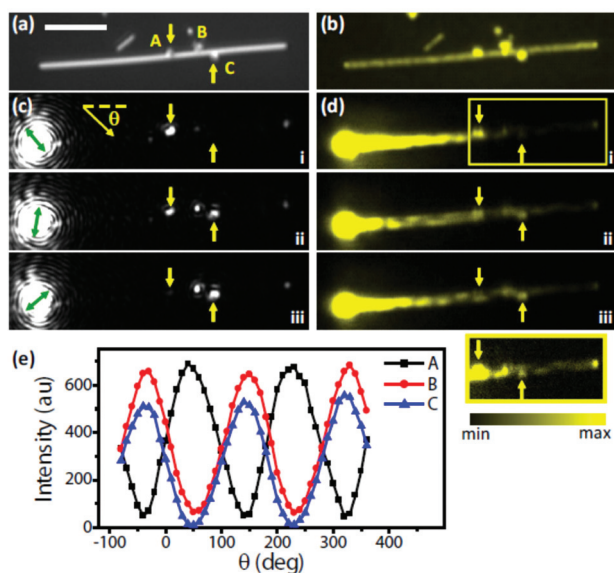


Fig. 3 (a) White light image of a NW–NP system. The length of the scale bar is 5 μm . (b) QD fluorescence image of the system for wide field illumination. (c) Scattering images of the propagating SPs on the NW under different excitation polarizations. (d) QD fluorescence images corresponding to (c). The inset at the bottom shows the part in the yellow rectangle in (d)i in a different contrast. (e) Scattering intensity of three NPs as a function of the incident laser polarization angle θ .

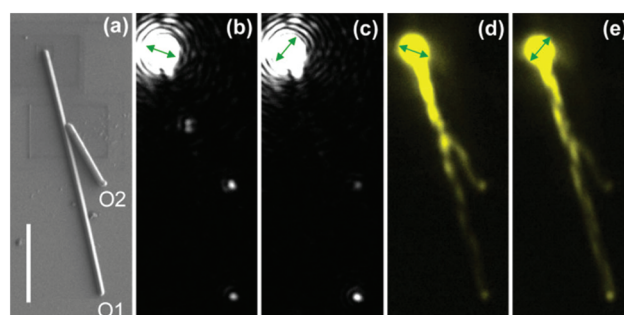


Fig. 4 (a) SEM image of a branched NW structure. The length of the scale bar is 5 μm . (b, c) Scattering images for two different laser polarizations indicated by the green arrows. (d, e) QD fluorescence images corresponding to (b, c). The main NW radius is 160 nm. The Al_2O_3 thickness is 30 nm.

dielectric environment shown in Fig. 1(a). The newly formed eigenmodes due to the introduction of substrate are denoted as H_0 , H_1 , H_2 , etc. Fig. 5(a) shows the four lowest order modes of a glass-supported Ag NW coated with 30 nm Al_2O_3 . The two lowest order modes H_0 and H_1 with large effective refractive indexes are mostly located within or close to the substrate, while the followed two higher order modes H_2 and H_3 have lower effective refractive indexes and the fields are mostly distributed in the air. The lower refractive indexes of H_2 and H_3 modes mean they are leaky modes with radiation into the glass substrate.

In Fig. 5(a), the directions of the field are also plotted. Because the structure preserved the symmetry in the horizontal direction, the modes are either symmetric or antisymmetric in this direction. The H_0 and H_2 modes here are analogues of the TM_0 mode, while H_1 and H_3 are analogues of the HE_1 mode. They can also be excited with the input light polarized parallel and perpendicular to the NW respectively. For input light polarized at a certain angle with respect to the NW, these modes can be generated simultaneously. Due to the serious leakage radiation, the H_3 mode can be neglected. Considering their polarization characteristics and difference in the effective refractive indexes, it can be determined that the superposition

of H_0 , H_1 and H_2 modes leads to the beating pattern on the NW. The routing of SPs in branched NW structures is determined by the field distribution near the junction. As shown in Fig. 5(b), changing the zigzag field distribution by tuning the laser polarization can manipulate the field at the junction and thus the routing of SPs in the NW network.

Al_2O_3 -cladding controlled plasmon routing

The plasmon modes are sensitive to the dielectric cladding of the NW, which can be used to control the plasmon propagation behavior in NW circuits. For the structure shown in Fig. 6(a), the output intensities at ends A and B show opposite polarization dependence (Fig. 6(b)). By depositing 5 nm of Al_2O_3 , the polarization dependences of both A and B are changed as shown in Fig. 6(c). Especially for end B, the polarization originally generating the strongest output intensity ($\theta \approx 230^\circ$) corresponds to the minimum output intensity after 5 nm Al_2O_3 deposited. Depositing an additional 5 nm of Al_2O_3 further changes the polarization dependence (Fig. 6(d)). The maximum output at end A corresponds to the minimum output at end B. Comparing Fig. 6(d) with Fig. 6(b), it can be seen that the polarization dependences for both ends A and B are reversed. These results show that the polarization dependence of the output light at the nanowire branches can be sensitively tuned by changing the dielectric coating thickness. Fig. 6(e) shows the scattering images for the original structure and after depositing 10 nm of Al_2O_3 . For the excitation polarization shown in Fig. 6(e), end A is at OFF state, and end B is at ON state for the original structure, that is, the plasmons are routed to the right branch. After depositing 10 nm Al_2O_3 , the plasmons are routed to the left branch, making end A switch to ON and end B switch to OFF for the same laser polarization. The QD fluorescence images in Fig. 6(f) reveal the change of the electric field distribution for the SPs on the NW. After depositing 10 nm of Al_2O_3 , the period of the near field pattern on the main wire is increased. Due to the change of the asymmetric field distribution on the main wire, the field intensity at the left junction becomes strong and that at the right junction becomes weak, which leads to the routing of the plasmon signal to end A and the switching off of the signal to end B.

Different from the plasmon routing controlled by the polarization of input light, the cladding-controlled plasmon routing is achieved because of the dependence of the plasmon field distribution on the thickness of the coating layer. By depositing a thin layer of Al_2O_3 onto the NW surface, the dielectric environment of the NW is changed, which changes the effective refractive indexes of the plasmon modes on the NW. The period of plasmon field distribution formed by two plasmon modes on the NW is determined by $\Lambda = \lambda/\Delta n$, where Λ is the plasmon field period, λ is the vacuum wavelength of the input light, and Δn is the difference of the effective refractive indexes for the two plasmon modes. Increasing the thickness of Al_2O_3 decreases the value of Δn , so that the plasmon field period is increased as the case in Fig. 6(f).³⁵ The increase of the period changes the local field intensity at the junctions of the two branches for the NW network in Fig. 6. Therefore, the

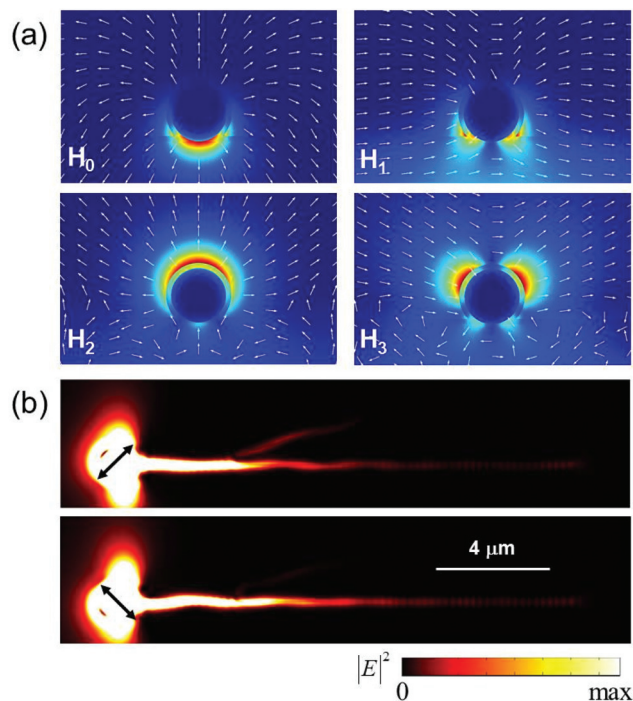


Fig. 5 Simulations for the experimental structure in Fig. 4. (a) The field amplitude distributions of the four lowest order modes supported by the structure. The NW radius is 160 nm and the Al_2O_3 thickness is 30 nm. (b) Field intensity distribution on a plane 5 nm above the Al_2O_3 layer on the branched NW, under excitation beam polarized with angles of 45° and 135° to the NW. The radius of the NWs is all 160 nm and the thickness of Al_2O_3 is 30 nm. Each end of the NW is capped by a hemisphere. The short branch is 16° with respect to the main wire. The junction is $4.35 \mu\text{m}$ away from the input terminal.

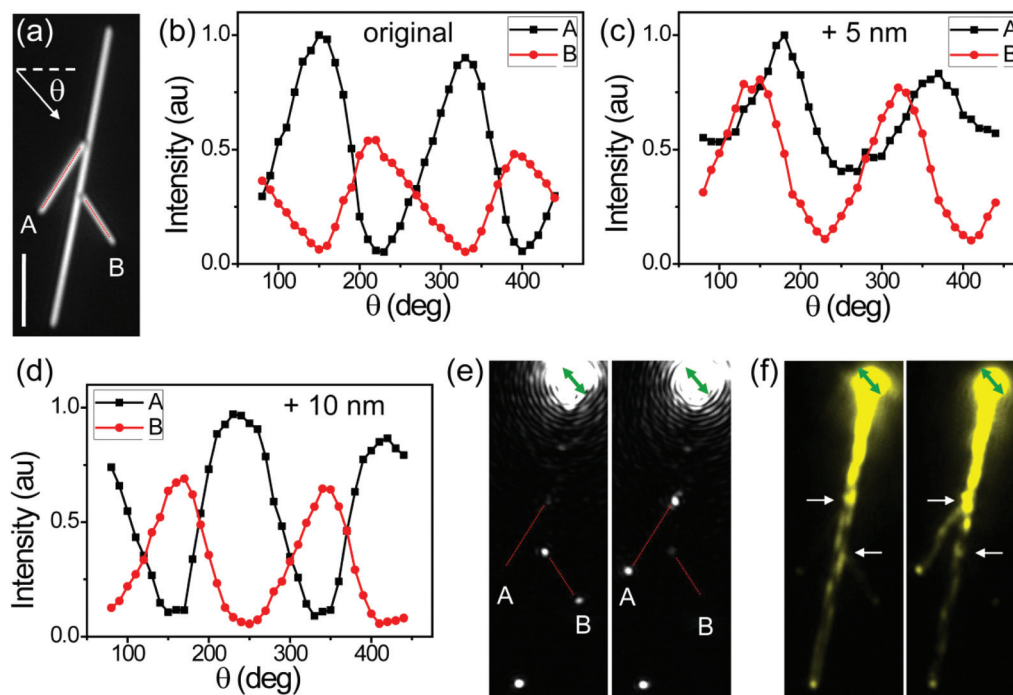


Fig. 6 (a) White light image of a NW network. The length of the scale bar is 5 μm . (b–d) Dependence of the output intensity at NW ends A and B on the polarization of the excitation light focused on the top end of the long wire for the original structure (b), for 5 nm (c) and 10 nm (d) Al₂O₃ layer deposited. The Al₂O₃ thickness of the original structure is 30 nm. The output intensities are normalized by the maximum values of the output intensity of terminal A. (e) Scattering images for the original structure and for 10 nm Al₂O₃ layer deposited with the same incident polarization indicated by the green arrows. (f) QD fluorescence images corresponding to (e). The red dot lines in (a) and (e) mark the branch wires. The white arrows in (f) are visual guides for the connection positions.

dependence of the output intensity on the laser polarization is changed. These results indicate that the function of a plasmonic NW network can be designed by choosing proper parameters for structural geometry and dielectric claddings. It is noted that apart from using a coating layer like Al₂O₃ to design passive plasmonic devices, active nanocircuits can also be developed by replacing the Al₂O₃ layer with materials with attractive characteristics such as optical nonlinear or electro-optical materials.

Conclusion

By experiments and simulations, we demonstrate that the surface plasmon routing in Ag nanowire networks is determined by the near field distribution formed by the excited plasmon modes. The near field distribution can be controlled by the incident laser polarization and dielectric coating. When the near field intensity at the junction of a branch wire is locally strong, more plasmons will be routed to that wire. The main nanowire can thus serve as a surface plasmon bus to distribute the electromagnetic energy/signals to different routes by managing the plasmon field arrangement. The manipulation to the near field distribution also provides a way to manage any near-field dependent processes. The controllable

and designable surface plasmon routing will benefit the development of plasmonic nanodevices and nanocircuits.

Acknowledgements

We thank Zhuoxian Wang and Xiaorui Tian for help in preparing the samples. We acknowledge the Laboratory of Microfabrication in the Institute of Physics, Chinese Academy of Sciences for experimental support. This work was supported by the Ministry of Science and Technology of China (Grant No. 2012YQ12006005 and 2015CB932400), the National Natural Science Foundation of China (Grant No. 11134013, 11227407, 11374012 and 11422436), the “Prominent Young Scientist Program” and the “Strategic Priority Research Program (B)” (Grant No. XDB07030100) of the Chinese Academy of Sciences.

References

- 1 H. Wei and H. X. Xu, *Mater. Today*, 2015, **17**, 372–380.
- 2 E. Ozbay, *Science*, 2006, **311**, 189–193.
- 3 R. M. Dickson and L. A. Lyon, *J. Phys. Chem. B*, 2000, **104**, 6095–6098.

- 4 B. Lamprecht, J. R. Krenn, G. Schider, H. Ditlbacher, M. Salerno, N. Felidj, A. Leitner, F. R. Aussenegg and J. C. Weeber, *Appl. Phys. Lett.*, 2001, **79**, 51–53.
- 5 D. F. P. Pile and D. K. Gramotnev, *Opt. Lett.*, 2004, **29**, 1069–1071.
- 6 D. F. P. Pile, T. Ogawa, D. K. Gramotnev, T. Okamoto, M. Haraguchi, M. Fukui and S. Matsuo, *Appl. Phys. Lett.*, 2005, **87**, 061106.
- 7 R. F. Oulton, V. J. Sorger, D. A. Genov, D. F. P. Pile and X. Zhang, *Nat. Photonics*, 2008, **2**, 496–500.
- 8 L. J. E. Anderson, Y. R. Zhen, C. M. Payne, P. Nordlander and J. H. Hafner, *Nano Lett.*, 2013, **13**, 6256–6261.
- 9 H. Ditlbacher, A. Hohenau, D. Wagner, U. Kreibig, M. Rogers, F. Hofer, F. R. Aussenegg and J. R. Krenn, *Phys. Rev. Lett.*, 2005, **95**, 257403.
- 10 A. W. Sanders, D. A. Routenberg, B. J. Wiley, Y. N. Xia, E. R. Dufresne and M. A. Reed, *Nano Lett.*, 2006, **6**, 1822–1826.
- 11 M. W. Knight, N. K. Grady, R. Bardhan, F. Hao, P. Nordlander and N. J. Halas, *Nano Lett.*, 2007, **7**, 2346–2350.
- 12 Z. Wu, H. M. Li, X. Xiong, G. B. Ma, M. Wang, R. W. Peng and N. B. Ming, *Appl. Phys. Lett.*, 2009, **94**, 041120.
- 13 H. Wei and H. X. Xu, *Nanophotonics*, 2012, **1**, 155–169.
- 14 X. Guo, Y. G. Ma, Y. P. Wang and L. M. Tong, *Laser Photonics Rev.*, 2013, **7**, 855–881.
- 15 X. Xiong, C. L. Zou, X. F. Ren, A. P. Liu, Y. X. Ye, F. W. Sun and G. C. Guo, *Laser Photonics Rev.*, 2013, **7**, 901–919.
- 16 Z. P. Li, F. Hao, Y. Z. Huang, Y. R. Fang, P. Nordlander and H. X. Xu, *Nano Lett.*, 2009, **9**, 4383–4386.
- 17 T. Shegai, V. D. Miljkovic, K. Bao, H. X. Xu, P. Nordlander, P. Johansson and M. Kall, *Nano Lett.*, 2011, **11**, 706–711.
- 18 Z. X. Wang, H. Wei, D. Pan and H. X. Xu, *Laser Photonics Rev.*, 2014, **8**, 596–601.
- 19 H. Wei, X. R. Tian, D. Pan, L. Chen, Z. L. Jia and H. X. Xu, *Nano Lett.*, 2015, **15**, 560–564.
- 20 Z. P. Li, K. Bao, Y. R. Fang, Y. Z. Huang, P. Nordlander and H. X. Xu, *Nano Lett.*, 2010, **10**, 1831–1835.
- 21 S. P. Zhang, H. Wei, K. Bao, U. Hakanson, N. J. Halas, P. Nordlander and H. X. Xu, *Phys. Rev. Lett.*, 2011, **107**, 096801.
- 22 Z. P. Li, K. Bao, Y. R. Fang, Z. Q. Guan, N. J. Halas, P. Nordlander and H. X. Xu, *Phys. Rev. B: Condens. Matter Mater. Phys.*, 2010, **82**, 241402.
- 23 W. H. Wang, Q. Yang, F. R. Fan, H. X. Xu and Z. L. Wang, *Nano Lett.*, 2011, **11**, 1603–1608.
- 24 M. X. Song, A. Bouhelier, P. Bramant, J. Sharma, E. Dujardin, D. G. Zhang and G. Colas-des-Francis, *ACS Nano*, 2011, **5**, 5874–5880.
- 25 S. P. Zhang and H. X. Xu, *ACS Nano*, 2012, **6**, 8128–8135.
- 26 Y. S. Bian and Q. H. Gong, *Nanoscale*, 2015, **7**, 4415–4422.
- 27 M. Allione, V. V. Temnov, Y. Fedutik, U. Woggon and M. V. Artemyev, *Nano Lett.*, 2008, **8**, 31–35.
- 28 C. Rewitz, T. Keitzl, P. Tuchscherer, J. Huang, P. Geisler, G. Razinskas, B. Hecht and T. Brixner, *Nano Lett.*, 2012, **12**, 45–49.
- 29 H. Wei and H. X. Xu, *Nanoscale*, 2012, **4**, 7149–7154.
- 30 H. Wei, Z. P. Li, X. R. Tian, Z. X. Wang, F. Z. Cong, N. Liu, S. P. Zhang, P. Nordlander, N. J. Halas and H. X. Xu, *Nano Lett.*, 2011, **11**, 471–475.
- 31 H. Wei, Z. X. Wang, X. R. Tian, M. Kall and H. X. Xu, *Nat. Commun.*, 2011, **2**, 387.
- 32 Z. P. Li, S. P. Zhang, N. J. Halas, P. Nordlander and H. X. Xu, *Small*, 2011, **7**, 593–596.
- 33 Y. R. Fang, Z. P. Li, Y. Z. Huang, S. P. Zhang, P. Nordlander, N. J. Halas and H. X. Xu, *Nano Lett.*, 2010, **10**, 1950–1954.
- 34 Q. Hu, D. H. Xu, Y. Zhou, R. W. Peng, R. H. Fan, N. X. Fang, Q. J. Wang, X. R. Huang and M. Wang, *Sci. Rep.*, 2013, **3**, 3095.
- 35 H. Wei, S. P. Zhang, X. R. Tian and H. X. Xu, *Proc. Natl. Acad. Sci. U. S. A.*, 2013, **110**, 4494–4499.
- 36 H. L. Qian, Y. G. Ma, Q. Yang, B. G. Chen, Y. Liu, X. Guo, S. S. Lin, J. L. Ruan, X. Liu, L. M. Tong and Z. L. Wang, *ACS Nano*, 2014, **8**, 2584–2589.
- 37 Z. Y. Fang, L. R. Fan, C. F. Lin, D. Zhang, A. J. Meixner and X. Zhu, *Nano Lett.*, 2011, **11**, 1676–1680.
- 38 S. P. Zhang, C. Z. Gu and H. X. Xu, *Small*, 2014, **10**, 4264–4269.
- 39 X. Guo, M. Qiu, J. M. Bao, B. J. Wiley, Q. Yang, X. N. Zhang, Y. G. Ma, H. K. Yu and L. M. Tong, *Nano Lett.*, 2009, **9**, 4515–4519.
- 40 R. X. Yan, P. Pausauskie, J. X. Huang and P. D. Yang, *Proc. Natl. Acad. Sci. USA*, 2009, **106**, 21045–21050.
- 41 Y. Fedutik, V. V. Temnov, O. Schops, U. Woggon and M. V. Artemyev, *Phys. Rev. Lett.*, 2007, **99**, 136802.
- 42 A. V. Akimov, A. Mukherjee, C. L. Yu, D. E. Chang, A. S. Zibrov, P. R. Hemmer, H. Park and M. D. Lukin, *Nature*, 2007, **450**, 402–406.
- 43 H. Wei, D. Ratchford, X. Q. Li, H. X. Xu and C. K. Shih, *Nano Lett.*, 2009, **9**, 4168–4171.
- 44 Q. Li, H. Wei and H. X. Xu, *Nano Lett.*, 2014, **14**, 3358–3363.
- 45 Q. Li, H. Wei and H. X. Xu, *Chin. Phys. B*, 2014, **23**, 097302.
- 46 R. Kolesov, B. Grotz, G. Balasubramanian, R. J. Stohr, A. A. L. Nicolet, P. R. Hemmer, F. Jelezko and J. Wrachtrup, *Nat. Phys.*, 2009, **5**, 470–474.
- 47 S. Kumar, N. I. Kristiansen, A. Huck and U. L. Andersen, *Nano Lett.*, 2014, **14**, 663–669.
- 48 T. Shegai, Y. Z. Huang, H. X. Xu and M. Kall, *Appl. Phys. Lett.*, 2010, **96**, 103114.
- 49 Y. G. Sun and Y. N. Xia, *Adv. Mater.*, 2002, **14**, 833–837.
- 50 P. B. Johnson and R. W. Christy, *Phys. Rev. B: Condens. Matter Mater. Phys.*, 1972, **6**, 4370–4379.
- 51 L. Allen, M. W. Beijersbergen, R. J. C. Spreeuw and J. P. Woerdman, *Phys. Rev. A*, 1992, **45**, 8185–8189.
- 52 D. Pan, H. Wei, Z. L. Jia and H. X. Xu, *Sci. Rep.*, 2014, **4**, 4993.